Asociación Argentina
de Mecánica Computacional

Mecánica Computacional Vol XXX, págs. 323-347 (artículo completo)
Oscar Möller, Javier W. Signorelli, Mario A. Storti (Eds.)
Rosario, Argentina, 1-4 Noviembre 2011

REENTRY FLOWS IN CHEMICAL NON-EQUILIBRIUM IN TWO-DIMENSIONS – PART II

Edisson Sávio de Góes Maciel

Mechanical Engineer/Researcher – Rua Demócrito Cavalcanti, 152 – Afogados – Recife – Pernambuco – Brazil – edissonsavio@yahoo.com.br

Keywords: Euler and Navier-Stokes equations, Reactive formulation, Chemical non-equilibrium, Hypersonic flow, Van Leer algorithm.

Abstract. This work, the second part of this study, presents a numerical tool implemented to simulate inviscid and viscous flows employing the reactive gas formulation of thermal equilibrium and chemical non-equilibrium. The Euler and Navier-Stokes equations, employing a finite volume formulation, on the context of structured and unstructured spatial discretizations, are solved. The aerospace problems involving the hypersonic flows around a double ellipse and around a reentry capsule, in two-dimensions, are simulated. As in the first part of this study was presented the structured formulation, in this paper, it will be presented the unstructured version to complete the reactive formulation. The reactive simulations will involve an air chemical model of five species: N, N_2, NO, O and O_2. Seventeen chemical reactions, involving dissociation and recombination, will be simulated. The Arrhenius formula will be employed to determine the reaction rates and the law of mass action will be used to determine the source terms. The algorithm employed to solve the reactive equations was the Van Leer, first- and second-order accurate ones. The second-order numerical scheme is obtained by a "MUSCL" ("Monotone Upstream-centered Schemes for Conservation Laws") extrapolation process in the structured case. In the unstructured case, tests with the linear reconstruction process did not yield converged results. The results have demonstrated that the most correct aerodynamic coefficient of lift, in the reentry capsule problem, is obtained by the Van Leer second-order accurate scheme in the viscous, structured simulation. The biggest aerodynamic coefficient of drag is obtained by the Van Leer first-order accurate scheme in the viscous, structured simulation. Moreover, the shock position is closer to the geometries as using the reactive formulation.

1 INTRODUCTION

In several aerodynamic applications, the atmospheric air, even being composed of several chemical species, can be considered as a perfect thermal and caloric gas due to its inert property as well its uniform composition in space and constancy in time. However, there are several practical situations involving chemical reactions, as for example: combustion processes, flows around spatial vehicles in reentry conditions or plasma flows, which do not permit the ideal gas hypothesis (Degrez and Van Der Weide, 1999). As described in Liu and Vinokur (1989), since these chemical reactions are very fast such that all processes can be considered in equilibrium, the conservation laws which govern the fluid become essentially unaltered, except that one equation to the general state of equilibrium has to be used opposed to the ideal gas law. When the flow is not in chemical equilibrium, one mass conservation law has to be written for each chemical species and the size of the equation system increases drastically.

Hypersonic flows are primary characterized by a very high level of energy (Saxena and Nair, 2005). Through the shock wave, the kinetic energy is transformed in enthalpy. The flow temperature between the shock wave and the body is very high. Under such conditions, the air properties are considerably modified. Phenomena like vibrational excitation and molecular dissociation of O_2 and N_2 frequently occur. The energy is stored under a form of free energy and the flow temperature is extremely reduced as compared with the temperature of an ideal gas flow. The thermodynamic and transport coefficients are not more constants. In summary, the ideal gas hypothesis is not truer and such flow is called the hypersonic flow of reactive gas or "hot gas flow".

As aforementioned, during the reentry and the hypersonic flights of aerospace vehicles in the atmosphere, reactive gas effects are present. The analysis of such hypersonic flows is critical to an appropriated aerodynamic and thermal project of such vehicles. The numerical simulation of reactive-gas-hypersonic flows is a very complex and disputed task. The present work emphasizes the numerical simulation of hypersonic flow in thermal equilibrium and chemical non-equilibrium.

Maciel and Pimenta (2010) have presented a work involving the numerical implementation of a tool to simulate inviscid and viscous flows employing the reactive gas formulation of thermal equilibrium and chemical non-equilibrium. The Euler and Navier-Stokes equations, employing a finite volume formulation, on the context of structured and unstructured spatial discretizations, were solved. The aerospace problem involving the hypersonic flow around a blunt body, in two-dimensions, was simulated. The reactive simulations involved an air chemical model of five species: N, N_2, NO, O and O_2. Seventeen chemical reactions, involving dissociation and recombination, were simulated. The Arrhenius formula was employed to determine the reaction rates and the law of mass action was used to determine the source terms of each gas species equation.

This work, the second part of the study started with Maciel and Pimenta (2010), presents a numerical tool implemented to simulate inviscid and viscous flows employing the reactive gas formulation of thermal equilibrium and chemical non-equilibrium flow in two-dimensions. The Euler and Navier-Stokes equations, employing a finite volume formulation, on the structured and unstructured spatial discretization contexts, are solved. The aerospace problems involving the "hot gas" hypersonic flow around a double ellipse and around a reentry capsule, in two-dimensions, are simulated. As in Maciel and Pimenta (2010) was presented the structured formulation of the two-dimensional Euler and Navier-Stokes reactive equations, in this paper it will be presented the unstructured version of the calculation algorithm in two-

dimensions to complete the formulation on structured and on unstructured contexts. The same chemical reactions and number of species, as described in Maciel and Pimenta (2010), are studied.

The algorithm employed to solve the reactive equations was the Van Leer (1982), first- and second-order accurate ones. The second-order numerical scheme is obtained by a MUSCL extrapolation process in the structured case (details in Hirsch, 1990). In the unstructured case, tests with the linear reconstruction process (details in Barth and Jespersen, 1989) did not yield converged results and, therefore, were not presented. The algorithm was implemented in a FORTRAN77 programming language, using the software Microsoft Developer Studio. Simulations in three microcomputers (one desktop and two notebooks) were accomplished: one with processor Intel Celeron of 1.5 GHz of clock and 1.0 GBytes of RAM (notebook), one with processor AMD-Sempron of 1.87 GHz of clock and 512 MBytes of RAM (desktop) and the third one with processor Intel Celeron of 2.13 GHz of clock and 1.0 GBytes of RAM (notebook).

The results have demonstrated that the most correct aerodynamic coefficient of lift, in the reentry capsule problem, is obtained by the Van Leer (1982) second-order accurate scheme in the viscous, structured simulation. The biggest aerodynamic coefficient of drag, in this problem, is obtained by the Van Leer (1982) first-order accurate scheme in the viscous, structured simulation. The cheapest algorithm was the unstructured Van Leer (1982) scheme, first-order accurate in space, to an inviscid simulation, as pointed in Maciel and Pimenta (2010). Moreover, the shock position is closer to the geometries as using the reactive formulation than the ideal gas formulation. It was verified in the inviscid and viscous cases.

2 FORMULATION TO REACTIVE FLOW IN THERMAL EQUILIBRIUM AND CHEMICAL NON-EQUILIBRIUM

The Navier-Stokes equations in thermal equilibrium and chemical non-equilibrium were implemented on a finite volume context, in the two-dimensional space. In this space, such equations in integral and conservative forms can be expressed by:

$$\frac{\partial}{\partial t}\int_V Q dV + \int_S \vec{F} \bullet \vec{n} dS = \int_V S_C dV \text{, with } \vec{F} = \left(E_e - E_v\right)\vec{i} + \left(F_e - F_v\right)\vec{j}, \quad (1)$$

where: Q is the vector of conserved variables, V is the computational cell volume, $\vec{F}$ is the complete flux vector, $\vec{n}$ is the normal unit vector to the flux face, S is the flux area, S_C is the chemical source term, E_e and F_e are the convective flux vectors or the Euler flux vectors in the x and y directions, respectively, and E_v and F_v are the viscous flux vectors in the x and y directions, respectively. The $\vec{i}$ and $\vec{j}$ unity vectors define the Cartesian coordinate system. Eight (8) conservation equations are solved: one of general mass conservation, two of linear momentum conservation, one of total energy and four of species mass conservation. Therefore, one of the species is absent of the iterative process. The CFD ("Computational Fluid Dynamics") literature recommends that the species to be omitted of the formulation should be that of biggest mass fraction of the gaseous mixture, aiming to result in the minimum accumulated numerical error, corresponding to the major constituent of the mixture (in the case, air). To the present study, in which is chosen an air chemical model composed of five (5) chemical species (N, N_2, NO, O and O_2) and seventeen (17) chemical reactions, being fifteen (15) dissociation reactions (endothermic reactions), this species can be the N_2 or the O_2. To this work, the O_2 was the chosen species. The Q, E_e, F_e, E_v, F_v and S_C vectors can,

hence, be defined as follows (Saxena and Nair, 2005):

$$Q=\begin{Bmatrix}\rho\\ \rho u\\ \rho v\\ e\\ \rho_1\\ \rho_2\\ \rho_3\\ \rho_4\end{Bmatrix},\ E_e=\begin{Bmatrix}\rho u\\ \rho u^2+p\\ \rho uv\\ \rho Hu\\ \rho_1 u\\ \rho_2 u\\ \rho_3 u\\ \rho_4 u\end{Bmatrix},\ F_e=\begin{Bmatrix}\rho v\\ \rho uv\\ \rho v^2+p\\ \rho Hv\\ \rho_1 v\\ \rho_2 v\\ \rho_3 v\\ \rho_4 v\end{Bmatrix},\ E_v=\frac{1}{\mathbf{Re}}\begin{Bmatrix}0\\ \tau_{xx}\\ \tau_{xy}\\ \tau_{xx}u+\tau_{xy}v-q_x-\phi_x\\ -\rho_1 v_{1x}\\ -\rho_2 v_{2x}\\ -\rho_3 v_{3x}\\ -\rho_4 v_{4x}\end{Bmatrix};\qquad(2)$$

$$F_v=\frac{1}{\mathbf{Re}}\begin{Bmatrix}0\\ \tau_{xy}\\ \tau_{yy}\\ \tau_{xy}u+\tau_{yy}v-q_y-\phi_y\\ -\rho_1 v_{1y}\\ -\rho_2 v_{2y}\\ -\rho_3 v_{3y}\\ -\rho_4 v_{4y}\end{Bmatrix}\quad\text{and}\quad S_C=\begin{Bmatrix}0\\ 0\\ 0\\ 0\\ \dot{\omega}_1\\ \dot{\omega}_2\\ \dot{\omega}_3\\ \dot{\omega}_4\end{Bmatrix},\qquad(3)$$

where: ρ is the mixture density; u and v are the Cartesian velocity components in the x and y directions, respectively; p is the fluid static pressure; e is the fluid total energy; ρ_1, ρ_2, ρ_3 and ρ_4 are the densities of the N, N_2, NO and O, respectively; H is the total enthalpy of the mixture; the τ's are the components of the viscous stress tensor; q_x and q_y are the components of the Fourier-heat-flux vector in the x and y directions, respectively; **Re** is the laminar Reynolds number of the flow; $\rho_s v_{sx}$ and $\rho_s v_{sy}$ represent the diffusion flux of the species, defined according to the Fick law; ϕ_x and ϕ_y are the terms of mixture diffusion; and $\dot{\omega}_s$ is the chemical source term of each species equation, defined by the law of mass action.

The viscous stresses, in N/m^2, are determined, following a Newtonian fluid model, by:

$$\tau_{xx}=2\mu\frac{\partial u}{\partial x}-\frac{2}{3}\mu\left(\frac{\partial u}{\partial x}+\frac{\partial v}{\partial y}\right),\ \tau_{xy}=\mu\left(\frac{\partial u}{\partial y}+\frac{\partial v}{\partial x}\right)\ \text{and}\ \tau_{yy}=2\mu\frac{\partial v}{\partial y}-\frac{2}{3}\mu\left(\frac{\partial u}{\partial x}+\frac{\partial v}{\partial y}\right),\qquad(4)$$

in which μ is the fluid molecular viscosity. The components of the Fourier-heat-flux vector, which considers only thermal conduction, are defined by:

$$q_x=-k\frac{\partial T}{\partial x}\quad\text{and}\quad q_y=-k\frac{\partial T}{\partial y}.\qquad(5)$$

The laminar Reynolds number is defined by:

$$\mathbf{Re}=\rho_\infty V_\infty L/\mu_\infty,\qquad(6)$$

where "∞" represents freestream properties, V_∞ represents the flow characteristic velocity and L is a characteristic length of the studied configuration. The species diffusion terms, defined by the Fick law, to a thermal equilibrium condition, are determined by (Saxena and Nair,

2005):

$$\rho_s v_{sx} = -\rho D \frac{\partial Y_s}{\partial x} \quad \text{and} \quad \rho_s v_{sy} = -\rho D \frac{\partial Y_s}{\partial y}, \tag{7}$$

with "s" referent to a given species, Y_s being the species mass fraction and D the binary diffusion coefficient of the mixture. The chemical-species-mass fraction "Y_s" is defined by:

$$Y_s = \rho_s / \rho \tag{8}$$

and the binary diffusion coefficient of the mixture is defined by:

$$D = \frac{kLe}{\rho Cp}, \tag{9}$$

where: k is the mixture thermal conductivity; Le is the Lewis number, kept constant to thermal equilibrium, with value 1.4 (Saxena and Nair, 2005); and Cp is the mixture specific heat at constant pressure. The ϕ_x and ϕ_y diffusion terms which appear in the energy equation are determined by (Saxena and Nair, 2005):

$$\phi_x = \sum_{s=1}^{ns} \rho_s v_{sx} h_s \quad \text{and} \quad \phi_y = \sum_{s=1}^{ns} \rho_s v_{sy} h_s, \tag{10}$$

being v_{sx} and v_{sy} the species diffusion velocities in the x and y directions, respectively; h_s the specific enthalpy (sensible) of the chemical species "s" and "ns" the total number of chemical species. The thermodynamic model, the transport model and the chemical model are described in Maciel and Pimenta (2010). As the unstructured algorithm of Van Leer (1982) was not presented in Maciel and Pimenta (2010), to complete the two-dimensional studies, this formulation is presented in section 3 of the present work.

3 UNSTRUCTURED ALGORITHM OF VAN LEER (1982) IN TWO-DIMENSIONS

To the numerical algorithm of Van Leer (1982) employing an unstructured formulation of the calculation domain, each rectangular cell of a structured computational mesh is transformed in two triangular cells to form an unstructured mesh by the use of connectivity, neighboring, ghost volume and nodes coordinate tables. Although the final mesh has not the benefits of a mesh really generated of unstructured way, the spatial discretization is unstructured and reliable results are obtained.

The numerical procedure to the unstructured algorithm of Van Leer (1982) is the same of the structured; in other words, the convective flux consists in uncouple the Euler equations in two parts, according to Ait-Ali-Yahia and Habashi (1997). One convective part associated with the dynamic flux of the reactive Euler equations and the other convective part associated with the chemical flux of the reactive Euler equations. The separation is described as follows.

The approximation to the integral equation (1) for a triangular finite volume yields a system of ordinary differential equations with respect to time defined by:

$$V_i \, dQ_i / dt = -R_i, \tag{11}$$

with R_i representing the net flux (residual) of mass conservation, general and of species, of the linear momentum conservation and of total energy in the volume V_i. One graphic representation of the triangular computational cell of volume V_i, with its nodes and respective flux interfaces and neighbors, is presented in Fig. 1. The volume V_i of the computational cell

described above is determined by:

$$V_i = 0.5\left|\left(x_{n1}y_{n2} + y_{n1}x_{n3} + x_{n2}y_{n3}\right) - \left(x_{n3}y_{n2} + y_{n3}x_{n1} + x_{n2}y_{n1}\right)\right|, \quad (12)$$

with n_1, n_2 and n_3 being the nodes of a given triangular cell, defined in Fig. 1. The cells ne1, ne2 and ne3 are the three neighbors of the triangular cell "i".

The connectivity table gives information about the three nodes: n1, n2 and n3, which defines a given triangular cell. The neighboring table gives information of the three neighbors that share the cell faces with the cell under study. The coordinate node table allows that the geometric properties of the mesh be calculated: cell volume, cell flux area, normal unity vector to the flux face, etc. The ghost cell table is related to boundary cells, referred in the CFD literature as "ghost" cells. Opposed to its three neighbors, in this table are indicated the unique real cell that share the computational domain boundary with the ghost cell and the type of ghost cell which are being used. In this work, the types of ghost cells vary from 1 to 4, being them: 1 – Wall ghost cell; 2 – Exit ghost cell; 3 – Entrance ghost cell; and 4 – Far field ghost cell.

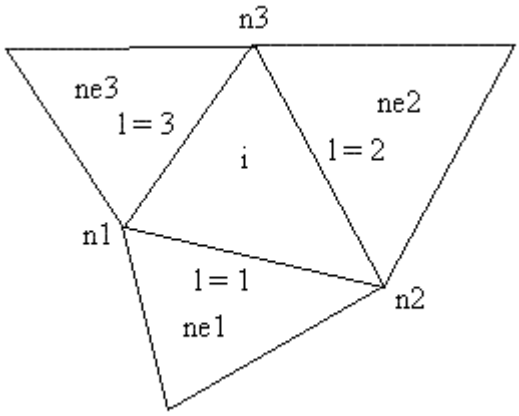

Figure 1: Unstructured Computational Cell, Its Nodes and Flux Interfaces.

The components of the unity vector normal to the flux interface and the area of the flux interface "l", n_x^l, n_y^l and S^l, are calculated as:

$$n_x^l = \Delta y_l / \left(\Delta x_l^2 + \Delta y_l^2\right)^{0.5},\ n_y^l = -\Delta x_l / \left(\Delta x_l^2 + \Delta y_l^2\right)^{0.5} \quad \text{and} \quad S^l = \left(\Delta x_l^2 + \Delta y_l^2\right)^{0.5}. \quad (13)$$

Expressions to Δx_l and Δy_l, on an unstructured context, are given in Tab. 1.

Interface	Δx_l	Δy_l
l = 1	$x_{n2} - x_{n1}$	$y_{n2} - y_{n1}$
l = 2	$x_{n3} - x_{n2}$	$y_{n3} - y_{n2}$
l = 3	$x_{n1} - x_{n3}$	$y_{n1} - y_{n3}$

Table 1: Values of Δx_l and Δy_l to the unstructured case.

The residual is calculated as:

$$R_i = R_1 + R_2 + R_3, \tag{14}$$

where $R_1 = R_1^e - R_1^v$, with "e" representing the residual associated with the flux of the Euler equations and "v" representing the residual associated with the viscous flux at the interface l = 1. The residuals are summed because the area components are considered with their respective coordinate signals.

As in the structured case (Maciel and Pimenta, 2009), the discrete flux of the Euler equations or the discrete convective flux calculated in this work follows the procedure described by the AUSM scheme (Advection Upstream Splitting Method) of Liou and Steffen Jr. (1993). This flux can be interpreted as a sum involving the arithmetical average between the right (R) and the left (L) states of the "l" cell face, involving cells "ne" and "i", respectively, multiplied by the interface Mach number, and a scalar dissipative term, as shown in Liou and Steffen Jr. (1993). Hence, the discrete-dynamic-convective-flux vector is defined by:

$$R_l = |S|_l \left\{ \frac{1}{2} M_l \left[\begin{pmatrix} \rho a \\ \rho a u \\ \rho a v \\ \rho a H \end{pmatrix}_L + \begin{pmatrix} \rho a \\ \rho a u \\ \rho a v \\ \rho a H \end{pmatrix}_R \right] - \frac{1}{2} \phi_l \left[\begin{pmatrix} \rho a \\ \rho a u \\ \rho a v \\ \rho a H \end{pmatrix}_R - \begin{pmatrix} \rho a \\ \rho a u \\ \rho a v \\ \rho a H \end{pmatrix}_L \right] \right\} + \begin{pmatrix} 0 \\ S_x p \\ S_y p \\ 0 \end{pmatrix}_l \tag{15}$$

and the discrete-chemical-convective-flux vector is defined by:

$$R_l = |S|_l \left\{ \frac{1}{2} M_l \left[\begin{pmatrix} \rho_1 a \\ \rho_2 a \\ \rho_3 a \\ \rho_4 a \end{pmatrix}_L + \begin{pmatrix} \rho_1 a \\ \rho_2 a \\ \rho_3 a \\ \rho_4 a \end{pmatrix}_R \right] - \frac{1}{2} \phi_l \left[\begin{pmatrix} \rho_1 a \\ \rho_2 a \\ \rho_3 a \\ \rho_4 a \end{pmatrix}_R - \begin{pmatrix} \rho_1 a \\ \rho_2 a \\ \rho_3 a \\ \rho_4 a \end{pmatrix}_L \right] \right\}, \tag{16}$$

where $S_l = \begin{bmatrix} S_x & S_y \end{bmatrix}_l^T$ defines the area vector normal to the flux interface "l", in which the area components are defined by: $S_x^l = n_x^l S^l$ and $S_y^l = n_y^l S^l$. The quantity "a" represents the sound speed, calculated as:

$$a = \sqrt{\gamma_f p/\rho}, \text{ for a thermal equilibrium formulation,} \tag{17}$$

being γ_f the frozen ratio of specific heats (details in Maciel, 2009 and 2010). M_l defines the advective Mach number at the face "l" of cell "i", which is calculated according to Liou and Steffen Jr. (1993) as:

$$M_l = M_L^+ + M_R^-, \tag{18}$$

where the separated Mach numbers, $M^{+/-}$, are defined by Van Leer (1982) as:

$$M^+ = \begin{cases} M, & \text{if } M \geq 1; \\ 0.25(M+1)^2, & \text{if } |M| < 1; \\ 0, & \text{if } M \leq -1; \end{cases} \quad \text{and} \quad M^- = \begin{cases} 0, & \text{if } M \geq 1; \\ -0.25(M-1)^2, & \text{if } |M| < 1; \\ M, & \text{if } M \leq -1. \end{cases} \tag{19}$$

M_L and M_R represent the Mach numbers associated with the left and right states, respectively. The advection Mach number is defined as:

$$M = \left(S_x u + S_y v\right) / \left(a|S|\right). \tag{20}$$

The pressure at face "l" of cell "i" is calculated in a similar way:

$$p_l = p_L^+ + p_R^-, \tag{21}$$

with $p^{+/-}$ representing the pressure separation defined according to Van Leer (1982):

$$p^+ = \begin{cases} p, & \text{if } M \geq 1; \\ 0.25p(M+1)^2(2-M), & \text{if } |M| < 1; \\ 0, & \text{if } M \leq -1; \end{cases} \quad \text{and} \quad p^- = \begin{cases} 0, & \text{if } M \geq 1; \\ 0.25p(M-1)^2(2+M), & \text{if } |M| < 1; \\ p, & \text{if } M \leq -1. \end{cases} \tag{22}$$

The definition of the dissipation term ϕ determines the particular formulation of the convective fluxes. The choice below corresponds to the Van Leer (1982) scheme, according to Radespiel and Kroll (1995):

$$\phi_l = \phi_l^{VL} = \begin{cases} |M_l|, & \text{if } |M_l| \geq 1; \\ |M_l| + 0.5(M_R - 1)^2, & \text{if } 0 \leq M_l < 1; \\ |M_l| + 0.5(M_L + 1)^2, & \text{if } -1 < M_l \leq 0. \end{cases} \tag{23}$$

The time integration is performed employing a Runge-Kutta explicit method of five stages, second-order accurate, for the two types of convective flux. To the dynamic part, this method can be represented in general form as:

$$\begin{aligned} Q_i^{(0)} &= Q_i^{(n)} \\ Q_i^{(k)} &= Q_i^{(0)} - \alpha_k \Delta t_i \, R\left(Q_i^{(k-1)}\right) / V_i \, , \\ Q_i^{(n+1)} &= Q_i^{(k)} \end{aligned} \tag{24}$$

and to the chemical part it can be represented in general form by:

$$\begin{aligned} Q_i^{(0)} &= Q_i^{(n)} \\ Q_i^{(k)} &= Q_i^{(0)} - \alpha_k \Delta t_i \left[R\left(Q_i^{(k-1)}\right) / V_i - S_C\left(Q_i^{(k-1)}\right)\right], \\ Q_i^{(n+1)} &= Q_i^{(k)} \end{aligned} \tag{25}$$

where k = 1,...,5; $\alpha_1 = 1/4$, $\alpha_2 = 1/6$, $\alpha_3 = 3/8$, $\alpha_4 = 1/2$ and $\alpha_5 = 1$. This scheme is first-order accurate in space and second-order accurate in time. The second-order of spatial accuracy is obtained by a linear reconstruction procedure (details in Barth and Jespersen, 1989).

The viscous formulation follows that of Long, Khan and Sharp (1991), which adopts the Green theorem to calculate primitive variable gradients. The viscous vectors are obtained by arithmetical average of flow properties between cell i and its neighbors. As was done with the convective terms, there is a need to separate the viscous flux in two parts: dynamical viscous flux and chemical viscous flux. The dynamical part corresponds to the first four equations of the Navier-Stokes ones and the chemical part corresponds to the last four equations. The scheme is accelerated to the steady state solution employing a spatially variable time step procedure, described in details in Maciel (2005a, 2008).

4 RESULTS

Tests were performed in three microcomputers. The criterion adopted to reach the steady

state was to consider a reduction of no minimal three (3) orders of magnitude in the value of the maximum residual in the calculation domain, a typical CFD community criterion. In the simulations, the attack angle was set equal to zero.

4.1 Initial and boundary conditions for the studied problems

The initial conditions are presented in Tab. 2 for the double ellipse and in Tab. 3 for the reentry capsule. The Reynolds number is obtained from data of Fox and McDonald (1988).

Property	Value
M_∞	15.0
ρ_∞	0.00922 kg/m^3
p_∞	794 Pa
U_∞	5,208 m/s
T_∞	300 K
altitude	50,000 m
Y_N	10^{-9}
Y_{N_2}	0.73555
Y_{NO}	0.05090
Y_O	0.07955
L	5.0 m
Re_∞	1.5778x10^6

Table 2: Initial conditions for the problem of the double ellipse.

Property	Value
M_∞	10.6
ρ_∞	0.02863 kg/m^3
p_∞	3,885 Pa
U_∞	4,628 m/s
T_∞	473 K
Altitude	40,000 m
Y_N	10^{-9}
Y_{N_2}	0.73555
Y_{NO}	0.05090
Y_O	0.07955
L	3.0 m
Re_∞	3.4718x10^6

Table 3: Initial conditions for the problem of the reentry capsule.

The boundary conditions of the double-ellipse-reactive-flow problem are detailed in Maciel (2009), being constituted of entrance, exit and wall boundaries. The boundary conditions of the reentry-capsule-reactive-flow problem are: entrance, exit, wall and continuity boundaries, where the last one guarantees the flow continuity at the configuration trailing edge (Kutta condition). The nondimensionalization employed in the Euler and Navier-Stokes equations in this study is also described in Maciel (2009).

4.2 Results of the double ellipse in thermal equilibrium and chemical non-equilibrium

Inviscid, structured and first-order accurate case. Figure 2 presents the pressure contours calculated in the computational domain. The pressure peak at the configuration nose reaches the non-dimensional value superior to 1,680 unities. The shock wave at the configuration nose is normal. A second shock wave develops at the minor ellipse. This second shock wave is weaker than the first one, as observed in the pressure contours. Figure 3 exhibits the Mach number contours obtained from the simulation. The normal shock at the configuration nose yields a subsonic flow region behind it. This region is also characterized at the second ellipse. The shock wave develops naturally passing from a normal shock wave until be attenuated to a Mach wave, far from de configuration.

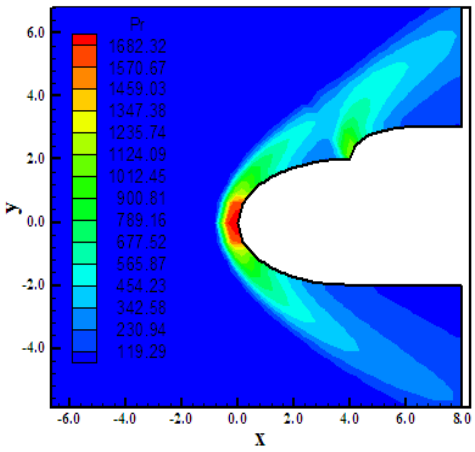

Figure 2: Pressure Contours.

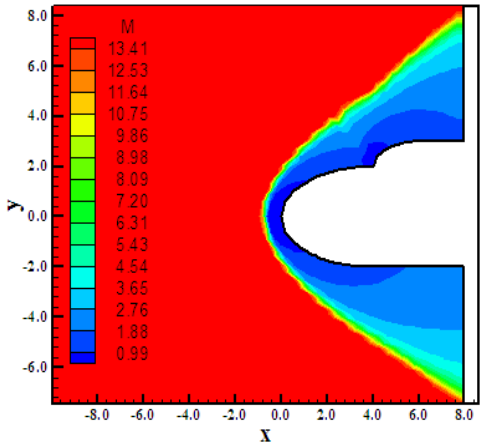

Figure 3: Mach Number Contours.

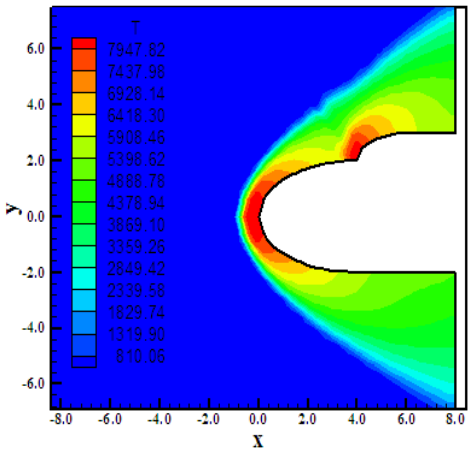

Figure 4: T/R Temperature Contours.

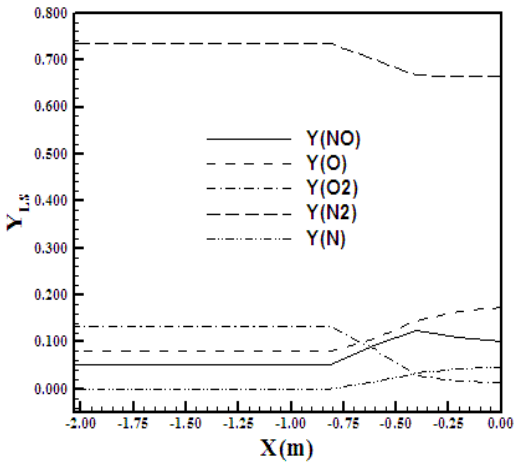

Figure 5: Mass Fraction Distribution at the Stagnation Line.

Figure 4 presents the contours of the distribution of the translational/rotational temperature (one temperature model) in the computational domain. The peaks of temperature at the configuration nose and at the second ellipse reach approximately 8,000 K. In these regions occur dissociation of the O_2 and N_2. Figure 5 presents the mass fraction distribution of the five chemical species of the study, namely: N, N_2, NO, O and O_2, along the line of stagnation of the geometry. As can be observed by the figure, a meaningful dissociation of the N_2 and O_2 occurs, as expected, with a consequent increase of the N, NO and O in the gaseous mixture.

The increase of the N presents a highlighted behavior, considering its initial value, and the increase of the O has also a meaningful aspect. It is interesting to note that the increase of the NO would be bigger at the configuration nose. However, due to the constancy reached by the mass fraction distribution of the N_2 and the increase in the formation of the N and O, at this region, caused a reduction in the NO formation.

Viscous, structured and first-order accurate case. Figure 6 shows the pressure contours calculated in the computational domain. The non-dimensional pressure peak at the configuration nose has a value of approximately 1,884 unities, bigger than that obtained to the inviscid case. Analyzing the complete pressure field, it is possible to note that it is more severe than its inviscid contra-part. The implemented code also captures the second shock wave at the minor ellipse. Figure 7 exhibits the Mach number contours calculated at the computational domain. The shock wave at the configuration nose is again normal, resulting in a subsonic region behind it. This subsonic region, due to the transport phenomena considered now, propagates until the second shock at the minor ellipse and to the double-ellipse-rectilinear walls. The shock wave also develops normally, passing from a normal shock wave to a Mach wave, more attenuated, far from the configuration.

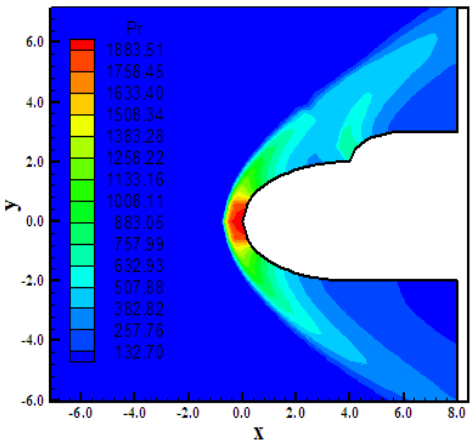

Figure 6: Pressure Contours.

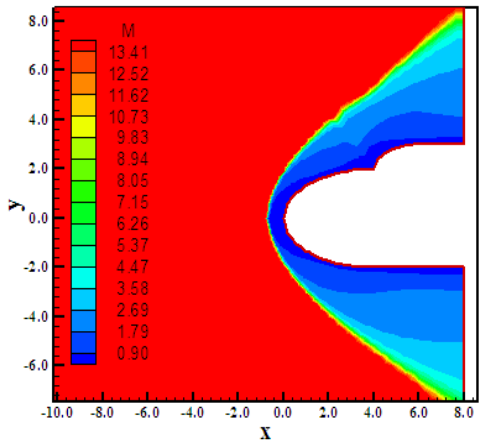

Figure 7: Mach Number Contours.

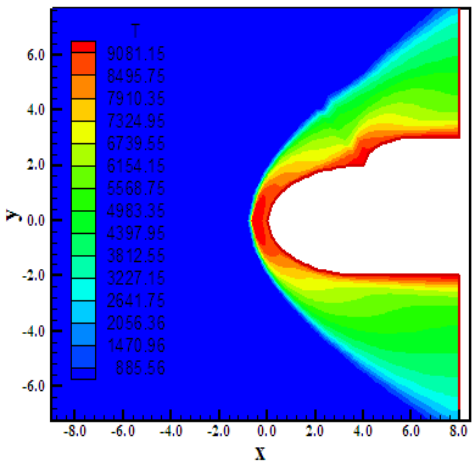

Figure 8: T/R Temperature Contours.

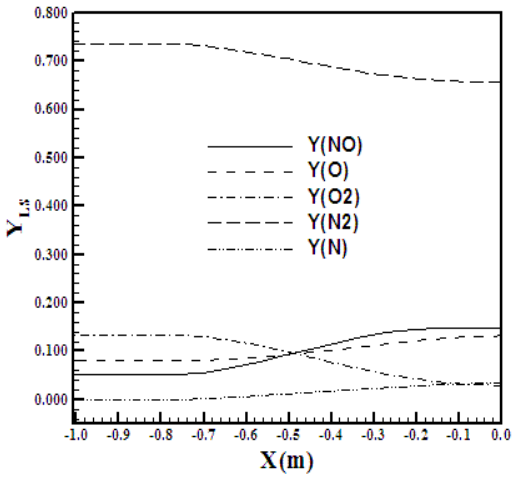

Figure 9: Mass Fraction Distribution at the Stagnation Line.

Figure 8 exhibits the contours of the translational/rotational temperature distribution calculated at the computational domain. At the double-ellipse-configuration nose and along

the geometry wall, the temperature reaches a maximum value superior to 9,000 K, which guarantees the dissociation of the O_2 and N_2. Figure 9 presents the mass fraction distribution of the five chemical species under study along the line of stagnation of the geometry. As can be observed by this figure, a meaningful dissociation of N_2 and O_2 occurs, as expected, with the consequent increase of the N, NO and O in the gaseous mixture. The increase of the NO presents a highlighted behavior. The formation of N is also considerable, taking into account its initial value, and the increase of O has also a meaningful behavior.

Inviscid, structured and second-order accurate case. Figure 10 exhibits the pressure contours to the problem of the double ellipse, employing the Van Leer (1982) scheme using the MUSCL procedure to obtain second-order accuracy. This MUSCL procedure employs a non-linear-flux-limiter type minmod. The pressure peak value is slightly inferior to the respective one obtained from the first-order structured solution. The pressure field is also less severe. The normal shock wave at the configuration nose is well captured, as also the second shock at the minor ellipse. Figure 11 shows the Mach number contours calculated at the computational domain. The normal shock wave generates a subsonic flow region behind it. Other region of subsonic flow is also manifested at the second ellipse. The shock wave presents its normal behavior, developing from the normal shock wave to a Mach wave.

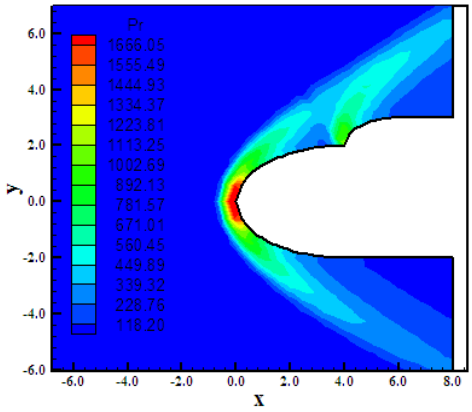

Figure 10: Pressure Contours.

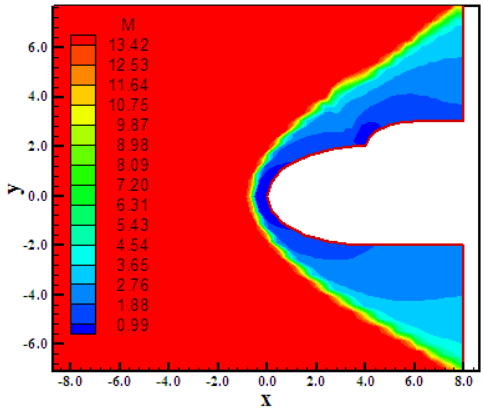

Figure 11: Mach Number Contours.

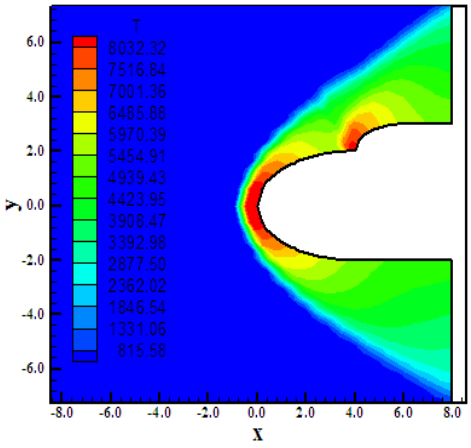

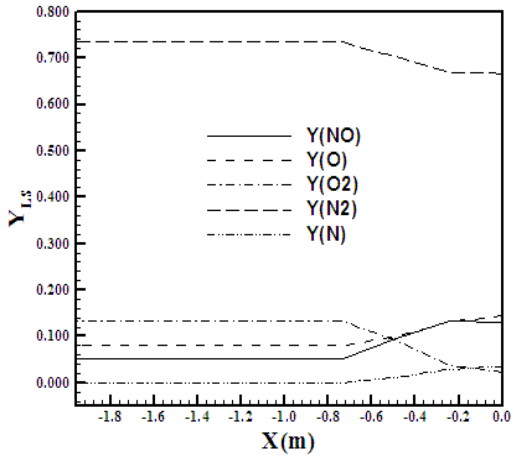

Figure 12: T/R Temperature Contours. Figure 13: Mass Fraction Distribution at the Stagnation Line.

Figure 12 presents the contours of the translational/rotational temperature distribution calculated at the computational domain. The temperature peak reaches approximately 8,000 K

at the configuration nose and at the minor ellipse. Dissociations of O_2 and N_2 in this region are expected. Behind the shock, all region present elevated values of temperature, which guarantee at least the dissociation of O_2. Figure 13 shows the mass fraction distribution of the five chemical species under study along the line of stagnation of the geometry. As can be observed by this figure, a meaningful dissociation of the N_2 and O_2 occurs, as expected, with the consequent increase of N, of NO and of O in the gaseous mixture. The increase of the NO presents a highlighted behavior. The formation of N is also considerable, taking into account its initial value, and the increase of O has also important behavior. This solution presented to the inviscid case of second-order is comparable to that obtained with the first-order solution, indicating that the behaviors of both solutions are equivalent.

Viscous, structured and second-order accurate case. Figure 14 shows the pressure contours to the problem of the double ellipse, in two-dimensions, considering viscous flow simulated with the Van Leer (1982) scheme of second-order TVD (Total Variation Diminishing). The non-dimensional pressure peak is approximately equal to 1,900 unities, bigger than the inviscid and viscous first-order solutions and than the inviscid second-order solution, representing the most severe pressure field. The pressure peak occurs at the double-ellipse-configuration nose. The second shock at the minor ellipse is also captured. Figure 15 exhibits the Mach number contours obtained at the computational domain. The subsonic region behind the normal shock is well characterized and propagates along the geometry wall. The expected behavior to the shock wave is ratified: normal shock, oblique shocks and Mach wave.

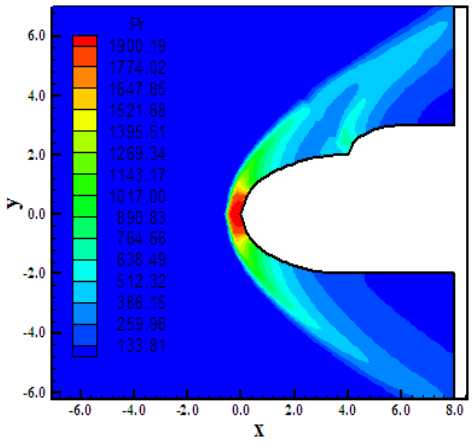

Figure 14: Pressure Contours.

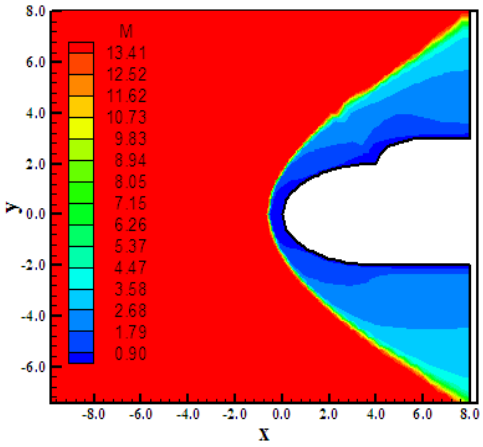

Figure 15: Mach Number Contours.

Figure 16 presents the translational/rotational temperature distribution calculated at the computational domain. The temperature peak at the configuration nose reaches 9,000 K, which characterizes bigger dissociation of O_2 and N_2, mainly of N_2. Behind the shock, all regions allow the dissociation of the O_2 and N_2, due to the range of temperature oscillates between 4,000 K and 9,000 K. Figure 17 presents the mass fraction distribution of the five chemical species of the study, namely: N, N_2, NO, O and O_2, along the line of stagnation of the geometry. As can be observed, meaningful dissociation of the N_2 and O_2 occurs, as expected, with the consequent increase of the N, of NO and of O in the gaseous mixture. The increase of the NO presents a highlighted behavior. The N formation is also considerable, as observed its initial value, and the increase of O has also meaningful behavior. This solution presented to the second-order viscous case is comparable to that obtained with the first-order solution, indicating that the behaviors of both solutions are equivalents.

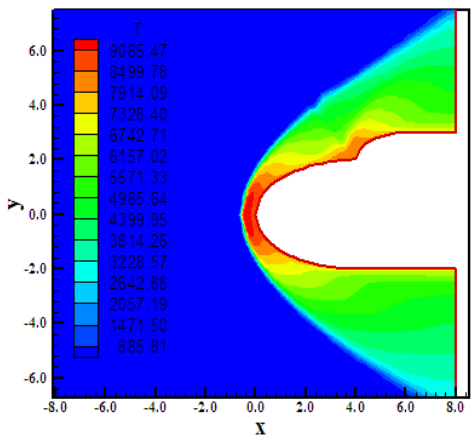

Figure 16: T/R Temperature Contours.

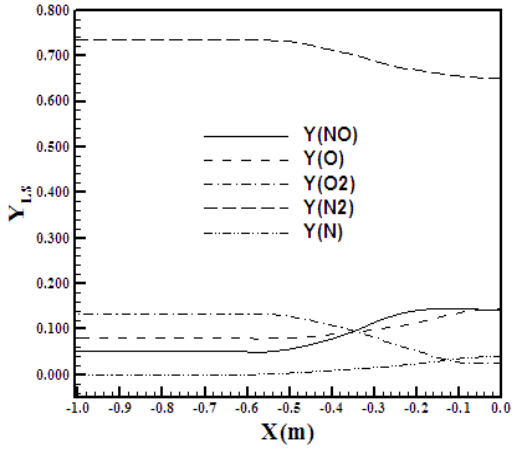

Figure 17: Mass Fraction Distribution at the Stagnation Line.

Inviscid, unstructured and first-order accurate case. Figure 18 presents the pressure contours obtained by the inviscid simulation, unstructured, of first-order, at the computational domain. The non-dimensional pressure peak, approximately 1,800 unities, is bigger than that obtained with the first-order inviscid structured solution. This peak occurs at the configuration nose. The second shock at the minor ellipse is well captured. Figure 19 exhibits the Mach number contours calculated at the computational domain. The subsonic region behind the normal shock is well characterized. In the second shock also appears a region of subsonic flow. The shock develops normally.

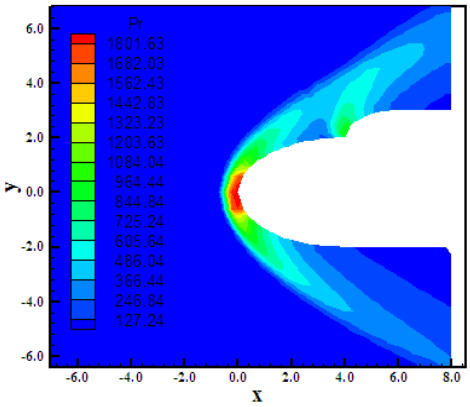

Figure 18: Pressure Contours.

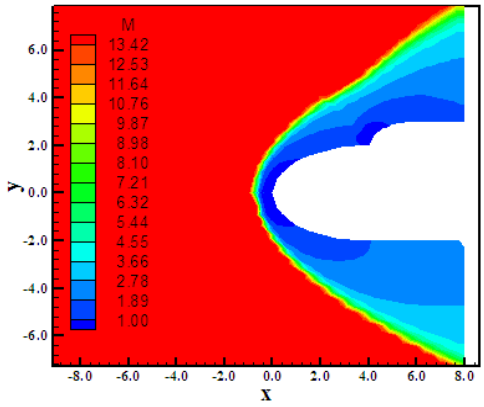

Figure 19: Mach Number Contours.

Figure 20 shows the translational/rotational temperature distribution around the double ellipse, calculated at the computational domain. The temperature peak at the regions of the configuration nose and at the minor ellipse presents an approximated value of 8,500 K, which guarantees good dissociation of N_2 and O_2 in these regions. Figure 21 exhibits the velocity vector field to the inviscid flow. The flow tangency condition is well assured by the employed inviscid formulation. It is not presented the mass fraction distribution along the line of stagnation in the unstructured case due to the difficult in determine this line in this case. On the other hand, the velocity vector field is presented.

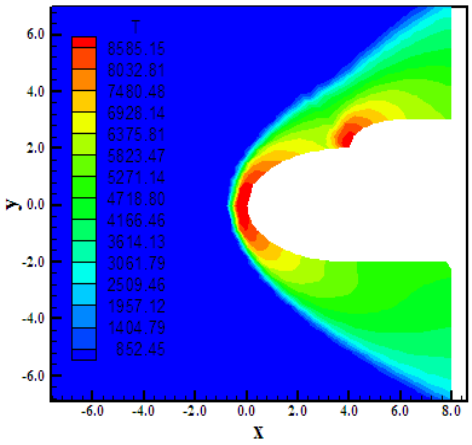

Figure 20: T/R Temperature Contours.

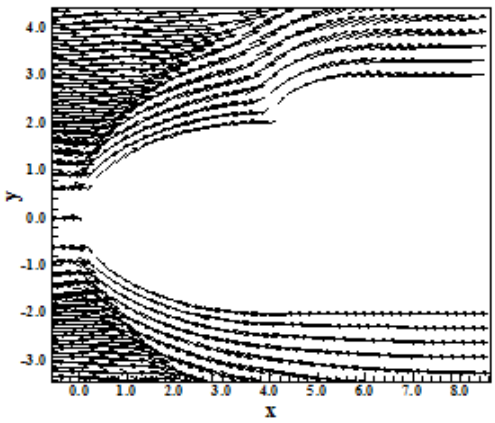

Figure 21: Velocity Vector Field.

Viscous, unstructured and first-order accurate case. Figure 22 presents the pressure contours calculated at the computational domain to this viscous case of the double ellipse, on an unstructured context. The pressure peak is bigger than those of the respective structured solutions of first- and second-order spatial accuracy. The pressure peak occurs at the configuration nose, where appears the normal shock. The second shock at the minor ellipse is well captured. Figure 23 shows the Mach number contours calculated at the computational domain. The region of subsonic flow, behind the shock, is well characterized along the geometry, due to the consideration of the transport phenomena (viscosity, thermal conductivity and gaseous diffusion). The behavior of the shock is also the expected: normal shock, which develops to oblique shocks and finishing in Mach wave.

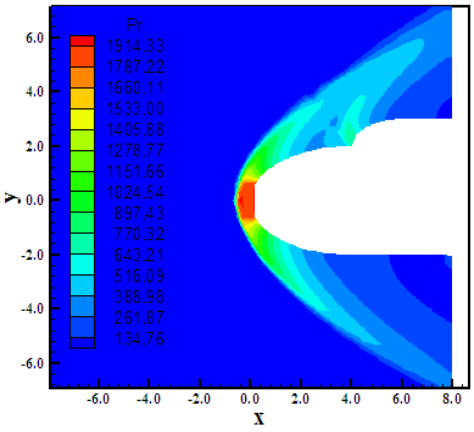

Figure 22: Pressure Contours.

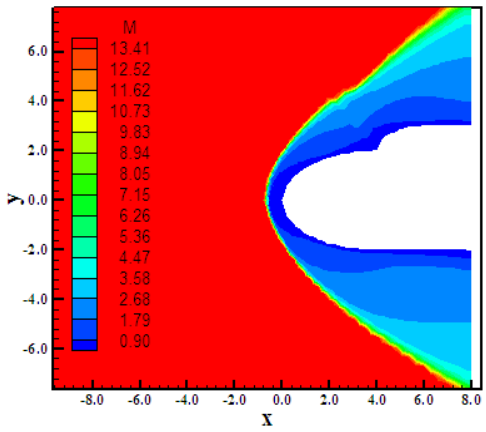

Figure 23: Mach Number Contours.

Figure 24 corresponds to the translational/rotational temperature distribution at the computational domain. The temperature peak at the configuration nose and at the minor ellipse is bigger than those obtained with the structured viscous first- and second-order solutions. This allows concluding that more dissociation of O_2 and N_2 will occurs. Figure 25 exhibits the velocity vector field to a flow viscous formulation. A small detachment of the boundary layer at the minor ellipse occurs, which, subsequently, is reattached. The adherence and impermeability conditions are guaranteed by the viscous formulation.

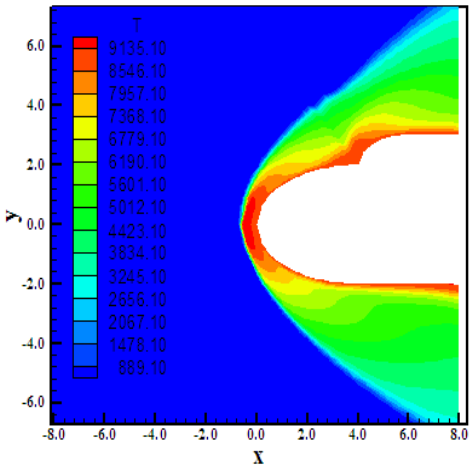

Figure 24: T/R Temperature Contours.

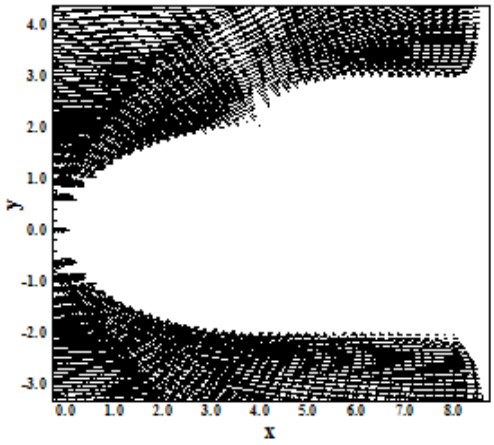

Figure 25: Velocity Vector Field.

4.3 Results of the reentry capsule in thermal equilibrium and chemical non-equilibrium

Inviscid, structured and first-order accurate case. Figure 26 presents the pressure contours calculated at the computational domain. The non-dimensional pressure peak is approximately equal to 1,261 unities. This peak is originated by the strong shock wave ahead of the reentry capsule geometry. Good symmetry characteristics are observed. Figure 27 exhibits the Mach number contours calculated at the computational domain. The normal shock ahead of the geometry generates a subsonic flow region behind it. Good characteristics of symmetry are observed. The shock presents the expected behavior: normal shock ahead of the geometry, followed by oblique shock waves and, finally, by a Mach wave far from the geometry.

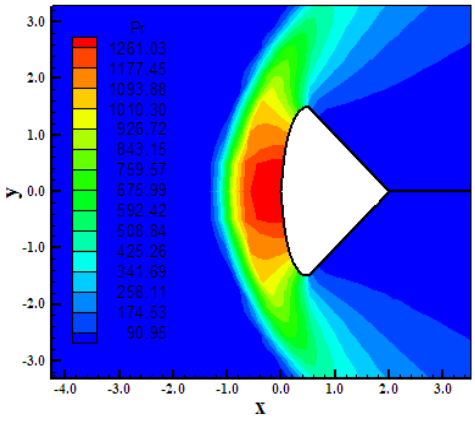

Figure 26: Pressure Contours.

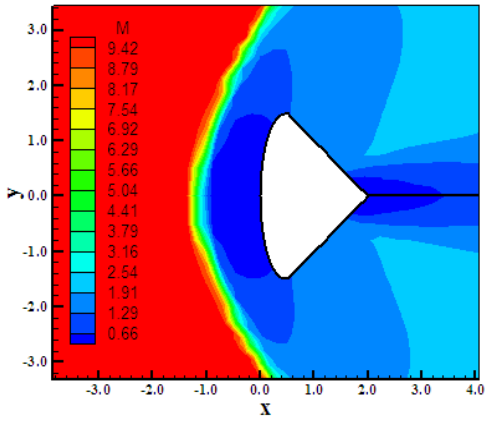

Figure 27: Mach Number Contours.

Figure 28 shows the translational/rotational temperature distribution calculated at the computational domain. The temperature peak reaches an approximated value of 7,100 K at the nose and at the configuration trailing edge. These regions present excellent characteristics of dissociation of the N_2 and of O_2. Figure 29 presents the mass fraction distribution of the five chemical species of the study, namely: N, N_2, NO, O and O_2, along the line of stagnation of the geometry. As can be observed, a meaningful dissociation of N_2 and of O_2 occurs, with subsequent increase of N, of NO and O in the gaseous mixture. The increase of N presents a meaningful behavior, considering its initial value, and the increase of O has also highlighted

behavior. It is interesting to note that the increase of NO would be bigger at the configuration nose. However, due to the constancy reached in the mass fraction of N_2 and the increase in the formation of N and O, the formation of NO is reduced close to the nose configuration.

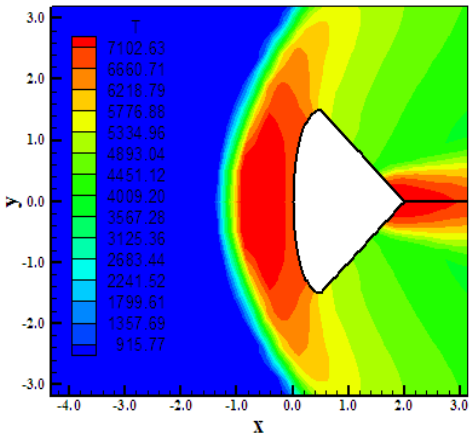

Figure 28: T/R Temperature Contours.

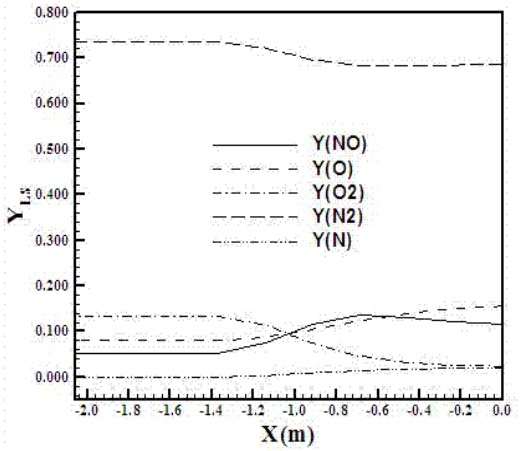

Figure 29: Mass Fraction Distribution at the Stagnation Line.

Viscous, structured and first-order accurate case. Figure 30 exhibits the pressure contours calculated at the computational domain. Due to the mesh refinement and the characteristics of the viscous reactive flow, the shock is closer to the geometry nose. The non-dimensional pressure peak assumes the value of 1,370 unities, superior to that obtained by the inviscid simulation. In other words, the viscous simulations in all studied examples of this work captured stronger shocks than the ones due to inviscid simulations. Good symmetry characteristics are observed. Figure 31 exhibits the Mach number contours obtained in this viscous simulation at the computational domain. The pos-shock subsonic region at the frontal region of the reentry capsule is well captured. A wake is formed at the geometry trailing edge. The shock develops normally: normal shock, oblique shocks and Mach wave.

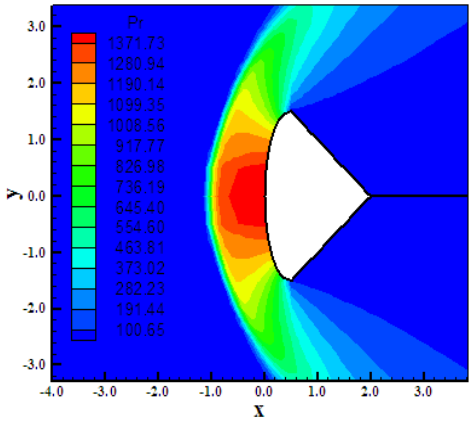

Figure 30: Pressure Contours.

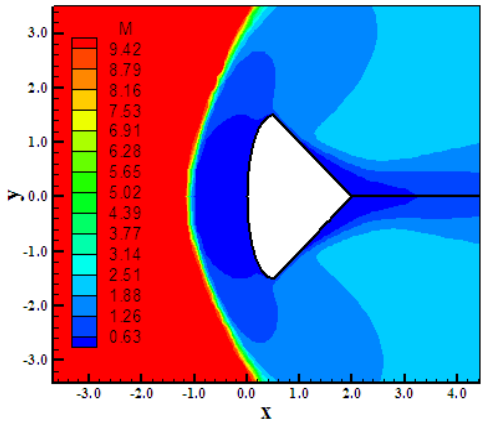

Figure 31: Mach Number Contours.

Figure 32 shows the contours of the translational/rotational temperature distribution calculated at the computational domain. The temperature reaches a peak of approximately 8,440 K at the configuration trailing edge. This is an indicative of great release of energy in this region, probably boundary layer separation to a viscous formulation, allowing the elevated dissociation of N_2 and O_2 and formation of N, NO and O. Even the configuration nose

presents elevated values of temperature, approximately 8,000 K, which allows concluding that this region is also of elevated dissociation of N_2 and O_2, with meaningful formation of N, NO and O. Figure 33 exhibits the velocity vector field to the reentry-capsule-viscous case. As can be observed, a boundary layer separation at the trailing edge of the reentry capsule occurs, in both lower and upper surfaces, allowing the appearance of a pair of circulation bubbles. As expected, this is a region of intense energy exchange and heating due to viscosity and thermal conductivity. Hence, the behavior observed in this problem relative to bigger production of N, NO and O at the reentry-capsule-trailing edge is justified.

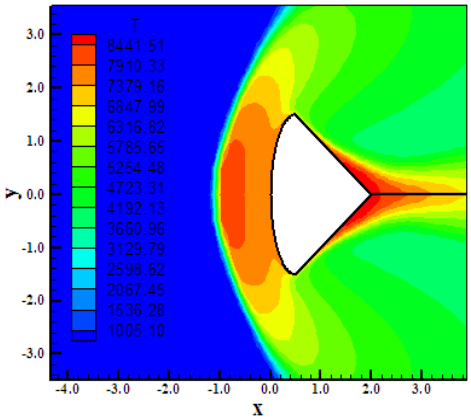

Figure 32: T/R Temperature Contours.

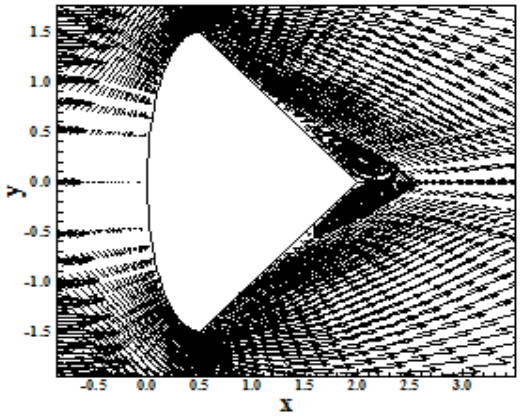

Figure 33: Streamlines in the Velocity Vector Field.

Figure 34 shows the mass fraction distribution of the five chemical species under study along the line of stagnation of the geometry. As can be observed, a meaningful dissociation of N_2 and of O_2 occurs, as expected by the temperature peak of approximately 8,000 K at the configuration nose, with the subsequent increase of N, of NO and of O in the gaseous mixture. The increase of N presents a more discrete behavior, but meaningful, considering its initial value, and the increase of O has a highlighted behavior. It is interesting to note that the increase of NO would be bigger at the configuration nose. However, due to the constancy reached by the mass fraction of N_2 and the increase in the formation of N and of O, a reduction in the formation of NO is characterized in this region.

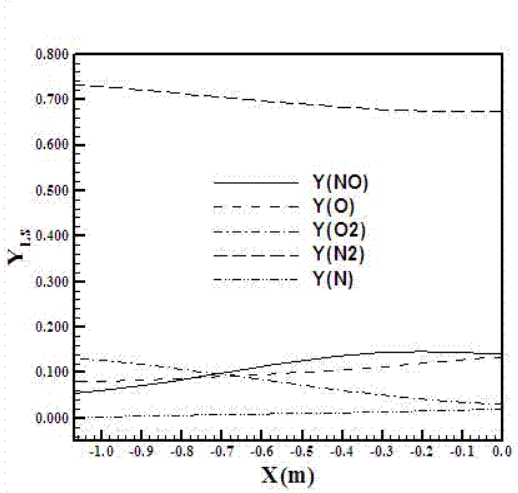

Figure 34: Mass Fraction Distribution at the Stagnation Line.

Inviscid, structured and second-order accurate case. Figure 35 exhibits the pressure contours

obtained by the inviscid simulation with the Van Leer (1982) scheme, employing a minmod non-linear flux limiter to obtain spatial second-order accuracy. The shock wave appears well defined and closer to the configuration nose than the first-order simulation. The non-dimensional pressure peak reaches a value close to 1,262 unities, slightly superior to that obtained with the first-order solution. Good symmetry characteristics are observed. Figure 36 shows the Mach number contours at the computational domain. The subsonic region behind the normal shock is formed. The shock behaves naturally, sweeping the configurations of normal shock until Mach wave.

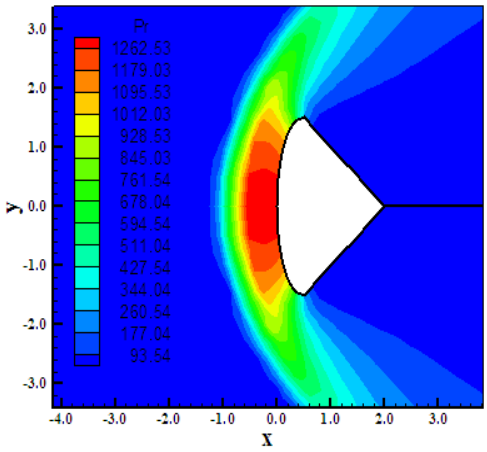

Figure 35: Pressure Contours.

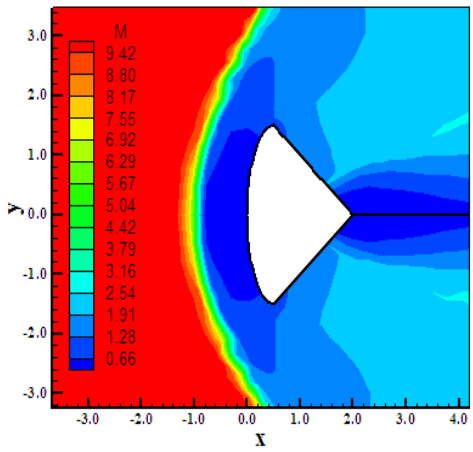

Figure 36: Mach Number Contours.

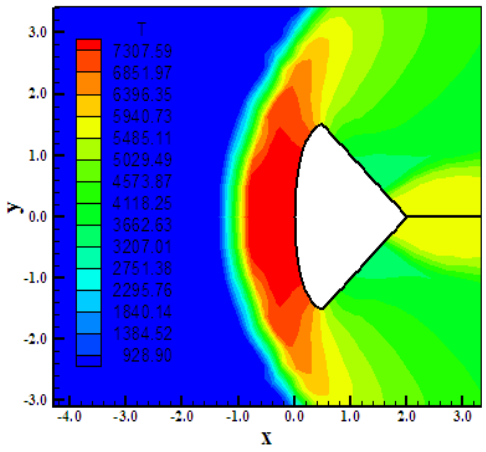

Figure 37: T/R Temperature Contours.

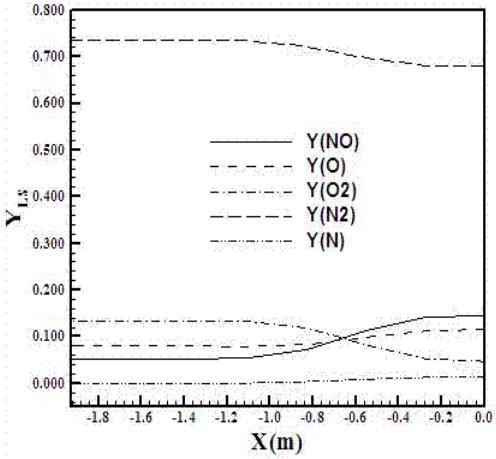

Figure 38: Mass Fraction Distribution at the Stagnation Line.

Figure 37 exhibits the contours of translational/rotational temperature distribution at the computational domain. The peak of temperature occurs at the configuration nose, approximately 7,300 K. This temperature allows a good dissociation of N_2 and O_2. Figure 38 presents the mass fraction distribution of the five chemical species under study, namely: N, N_2, NO, O and O_2, along the line of stagnation of the geometry. As can be observed, a meaningful dissociation of N_2 and of O_2 occurs, as expected, with the consequent increase of N, of NO and of O in the gaseous mixture. The increase of N is meaningful, considering its initial value, and the increase of O has also a highlighted behavior. The maximum increase was in the formation of the NO.

Viscous, structured and second-order accurate case. Figure 39 presents the pressure contours of the reentry capsule obtained by the viscous case, with second-order accuracy, studied in this work. The non-dimensional pressure peak is approximately equal to 1,346 unities, inferior to the respective obtained in the first-order case. The complete pressure field is less severe than that obtained with the first-order scheme, for the viscous case. The pressure contours present good symmetry characteristics. Figure 40 exhibits the Mach number contours calculated in the computational domain. A subsonic region behind the normal shock is formed and propagates until the wake, formed at the configuration trailing edge.

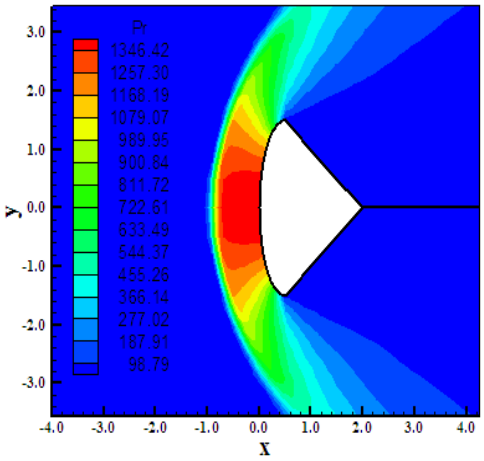

Figure 39: Pressure Contours.

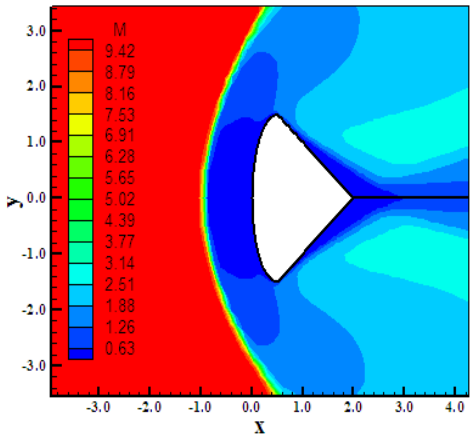

Figure 40: Mach Number Contours.

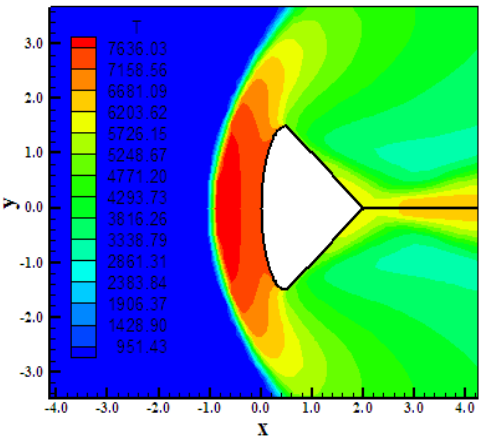

Figure 41: T/R Temperature Contours.

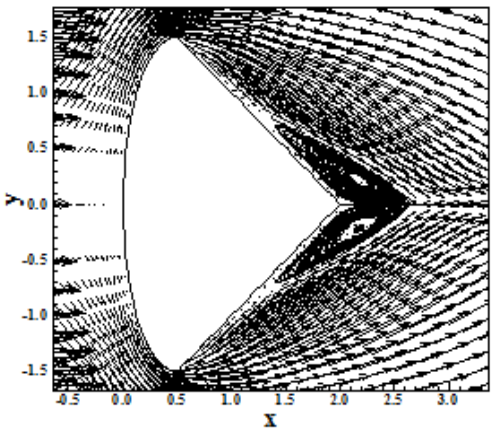

Figure 42: Streamlines in the Velocity Vector Field.

Figure 41 shows the contours of the translational/rotational temperature distribution at the computational domain. The temperature peak reaches approximately 7,600 K at the configuration nose. It is expected a good dissociation of N_2 and O_2. A wake less intense than that observed in the first-order solution is verified. Values of temperature in a range of 6,000 K are expected in this region, with mainly good dissociation of O_2 and reasonable dissociation of N_2. Figure 42 presents the velocity vector field obtained by the viscous formulation. As observed, a formation of a viscous wake is obtained from the solution. This wake is originated from the boundary layer detachment close to the trailing edge, with consequent formation of a pair of circulation bubbles. This happens because of in the geometry back side, there are the wall skin friction due to viscosity and a severe adverse pressure gradient due to the wall

inclination. These two factors contribute to the boundary layer detachment close to the configuration trailing edge.

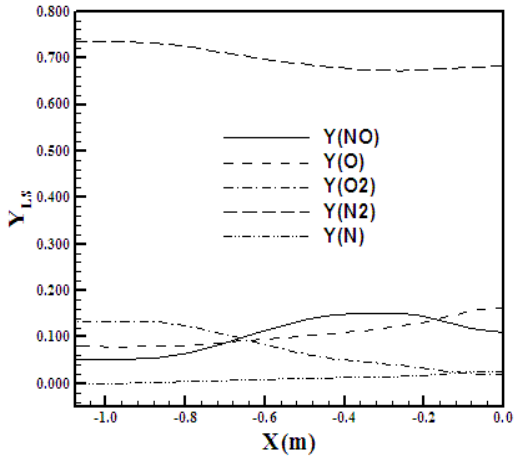

Figure 43: Mass Fraction Distribution at the Stagnation Line.

Figure 43 presents the mass fraction distribution of the five chemical species studied in this work, namely: N, N_2, NO, O and O_2, along the line of stagnation of the geometry. As can be observed by the figure, a meaningful dissociation of N_2 and of O_2 occurs, as expected by the temperature peak of approximately 7,600 K at the configuration nose, with the consequent increase of N, of NO and of O in the gaseous mixture. The increase of N presents a highlighted behavior, considering its initial value, and the increase of O has also an important behavior. It is interesting to note that the increase of NO should be bigger at the configuration nose. However, due to a slightly increase in the mass fraction of N_2 (recombination) and the increase in the formation of N and O, the formation of NO is reduced.

4.4 Shock position

In this section is presented the behavior of the shock position in ideal and in thermal equilibrium and chemical non-equilibrium conditions. Only first-order solutions are compared because the second-order ideal gas solutions did not present converged ones.

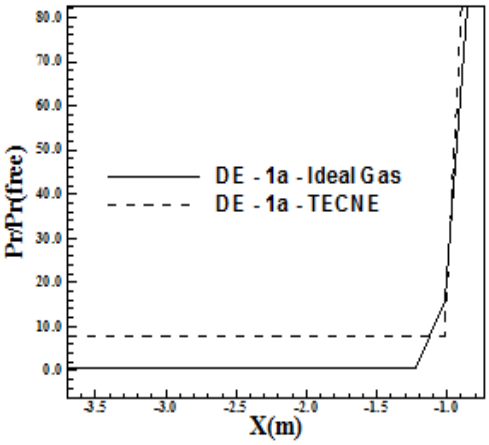

Figure 44: Shock Detachment (Inviscid Case).

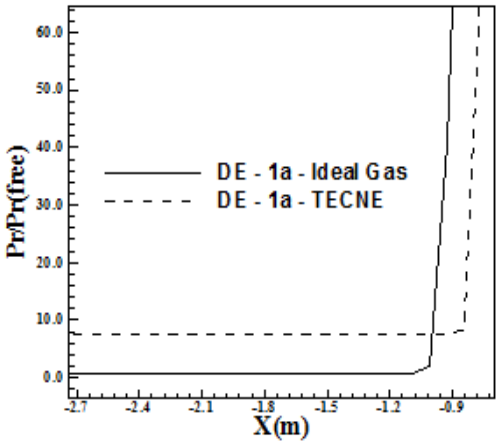

Figure 45: Shock Detachment (Viscous Case).

The detached shock position in terms of pressure distribution to the double ellipse problem,

in the inviscid case and first-order accurate solution, is exhibited in Fig. 44. It is shown the ideal-gas-shock position and the thermal equilibrium and chemical non-equilibrium shock position. As can be observed, the ideal-gas-shock position is located at 1.20 m, whereas the thermal equilibrium and chemical non-equilibrium position is located at 1.00 m. As referred in the CFD literature, in reactive flow the shock is closer to the configuration. As can be observed in this inviscid solution, the reactive shock is actually closer to the double ellipse.

The detached shock position in terms of pressure distribution to the double ellipse problem, in the viscous case and first-order accurate solution, is exhibited in Fig. 45. It is shown the ideal-gas-shock position and the thermal equilibrium and chemical non-equilibrium shock position. As can be observed, the ideal-gas-shock position is located at 1.02 m, whereas the thermal equilibrium and chemical non-equilibrium position is located at 0.84 m. As mentioned above, in reactive flow the shock is closer to the configuration. As can be observed in this viscous solution, the reactive shock is actually closer to the double ellipse.

The detached shock position in terms of pressure distribution to the reentry capsule problem, in the inviscid case and first-order accurate solution, is exhibited in Fig. 46. It is shown the ideal-gas-shock position and the thermal equilibrium and chemical non-equilibrium shock position. As can be observed, the ideal-gas-shock position is located at 1.85 m, whereas the thermal equilibrium and chemical non-equilibrium position is located at 1.60 m. As referred in the CFD literature, in reactive flow the shock is closer to the configuration. As can be observed in this inviscid solution, the reactive shock is actually closer to the reentry capsule than the ideal shock.

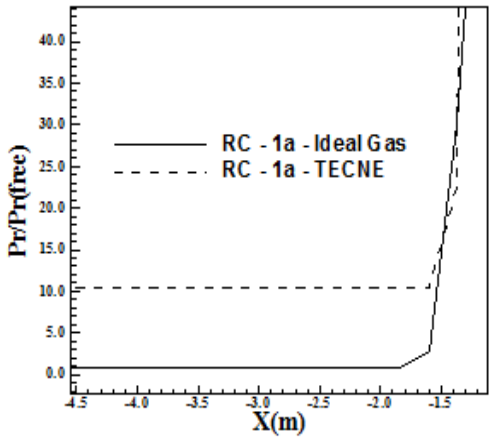

Figure 46: Shock Detachment (Inviscid Case).

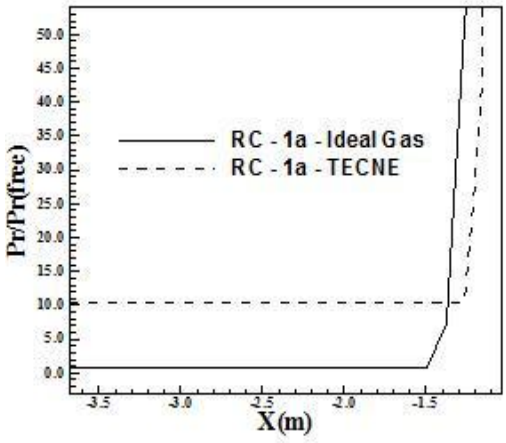

Figure 47: Shock Detachment (Viscous Case).

The detached shock position in terms of pressure distribution to the reentry capsule problem, in the viscous case and first-order accurate solution, is exhibited in Fig. 47. It is shown the ideal-gas-shock position and the thermal equilibrium and chemical non-equilibrium shock position. As can be observed, the ideal-gas-shock position is located at 1.50 m, whereas the thermal equilibrium and chemical non-equilibrium position is located at 1.30 m. As mentioned above, in reactive flow the shock is closer to the configuration. As can be observed in this viscous solution, the reactive shock is actually closer to the reentry capsule.

4.5 Aerodynamic coefficients of lift and drag

Table 4 exhibits the aerodynamic coefficients of lift and drag obtained by the problem of the reentry capsule, with structured discretization, for the reactive formulation. These

coefficients are due to the pressure term alone. The contribution of the friction term was not considered. To the problem of the reentry capsule, a symmetric geometry in relation to the x axis, a zero value is expected for the lift coefficient. By Table 4, it is possible to note that the solution closest to this value for c_L was that of the Van Leer (1982) scheme with second-order accuracy, in a viscous formulation. The maximum c_D was obtained by the solution of the Van Leer (1982) scheme, first-order accurate and employing a viscous formulation.

Studied Case	$\mathbf{c_L}$	$\mathbf{c_D}$
First-Order/Inviscid/TECNE(1)	5.616×10^{-4}	28.76
First-Order/Viscous/TECNE	1.718×10^{-4}	31.30
Second-Order/Inviscid/TECNE	-2.496×10^{-4}	28.76
Second-Order/Viscous/TECNE	1.079×10^{-4}	31.00

(1) TECNE: Thermal Equilibrium and Chemical Non-Equilibrium.

Table 4: Aerodynamic coefficients of lift and drag to the structured reentry capsule case.

4.6 Computational performance of the studied algorithm

Table 5 presents the computational data of the reactive simulations performed with the Van Leer (1982) scheme to the problem of the double ellipse in two-dimensions. In this table are exhibited the studied case, the maximum number of CFL employed in the simulation, the number of iterations to convergence and the number of orders of reduction in the magnitude of the maximum residual in relation to its initial value for convergence. As can be observed, the first-order test cases converged with no minimal four orders of reduction in the value of the maximum residual. The second-order cases converged with three orders of reduction in the value of the maximum residual. The maximum numbers of CFL presented the following distribution: 0.2 in two (2) cases (33.33%) and 0.1 in four (4) cases (66.67%). The convergence iterations did not overtake 10,000, in all studied cases. However, the time wasted in the simulations was much raised, taking until days to convergence (to four orders of reduction in the maximum residual and viscous cases). This can be verified in Maciel (2009).

Studied Case	**CFL**	**Iterations**	**Orders of Reduction of the Residual**
First-Order/Structured/Inviscid/2D/TECNE(1)	0.2	1,470	4
First-Order/Structured/Viscous/2D/TECNE	0.1	7,831	4
Second-Order/Structured/Inviscid/2D/TECNE	0.1	2,042	3
Second-Order/Structured/Viscous/2D/TECNE	0.1	5,704	3
First-Order/Unstructured/Inviscid/2D/TECNE	0.2	2,844	4
First-Order/Unstructured/Viscous/2D/TECNE	0.1	9,146	4

(1) TECNE: Thermal Equilibrium and Chemical Non-Equilibrium.

Table 5: Computational data of the reactive simulations of the double ellipse.

Table 6 presents the computational data of the reactive simulations performed with the Van Leer (1982) scheme to the problem of the reentry capsule in two-dimensions. In this table are exhibited the same parameters as in the double ellipse case (Tab. 5). As can be observed, half of the test cases (first-order solutions) converged with no minimal four orders of reduction in the value of the maximum residual and the other half of the test cases (second-order solutions) converged with no minimal three orders of reduction in the value of the maximum residual.

The maximum numbers of CFL presented the following distribution: 0.4 in one (1) case (25.00%) and 0.1 in three (3) case (75.00%). The convergence iterations did not overtake 9,000, in all studied cases. However, the time wasted in the simulations was much raised, taking until days to convergence (to four orders of reduction in the maximum residual and viscous cases). This aspect can be verified in Maciel (2009). It is important to emphasize that all two-dimensional viscous simulations were considered laminar, without the introduction of a turbulence model, although high Reynolds number were employed in the simulations.

Studied Case	CFL	Iterations	Orders of Reduction of the Residual
First-Order/Structured/Inviscid/2D/TECNE(1)	0.4	1,132	4
First-Order/Structured/Viscous/2D/TECNE	0.1	8,572	4
Second-Order/Structured/Inviscid/2D/TECNE	0.1	4,944	3
Second-Order/Structured/Viscous/2D/TECNE	0.1	5,161	3

(1) TECNE: Thermal Equilibrium and Chemical Non-Equilibrium.

Table 6: Computational data of the reactive simulations of the reentry capsule.

5 CONCLUSIONS

This work, the second part of the study started with Maciel and Pimenta (2010), presents a numerical tool implemented to simulate inviscid and viscous flows employing the reactive gas formulation of thermal equilibrium and chemical non-equilibrium flow in two-dimensions. The Euler and Navier-Stokes equations, employing a finite volume formulation, on the structured and unstructured spatial discretization contexts, are solved. The aerospace problems involving the "hot gas" hypersonic flow around a double ellipse and around a reentry capsule, in two-dimensions, are simulated. As in Maciel and Pimenta (2010) was presented the structured formulation of the two-dimensional Euler and Navier-Stokes reactive equations, in this paper it will be presented the unstructured version of the calculation algorithm in two-dimensions to complete the formulation on structured and on unstructured contexts.

To the simulations with unstructured spatial discretization, a structured mesh generator developed by the first author (Maciel, 2004), which create meshes of quadrilaterals (2D), was employed. After that, as a pre-processing stage (Maciel, 2005b), such meshes were transformed in meshes of triangles. Such procedure aimed to avoid the time which would be waste with the implementation of an unstructured generator, which was not the objective of the present work, and to obtain a generalized solver for the solution of the reactive equations.

The results have demonstrated that the most correct aerodynamic coefficient of lift, in the reentry capsule problem, is obtained by the Van Leer (1982) second-order accurate scheme in the viscous, structured simulation. The biggest aerodynamic coefficient of drag, in this problem, is obtained by the Van Leer (1982) first-order accurate scheme in the viscous, structured simulation. The cheapest algorithm was the unstructured Van Leer (1982) scheme, first-order accurate in space, to an inviscid simulation, as pointed in Maciel and Pimenta (2010). Moreover, the shock position is closer to the geometries as using the reactive formulation than the ideal gas formulation. It was verified in the inviscid and viscous cases.

REFERENCES

Ait-Ali-Yahia, D., and Habashi, W. G., Finite Element Adaptive Method for Hypersonic Thermochemical Nonequilibrium Flows. *AIAA Journal*, 35(8): 1294-1302, 1997.

Barth, T. J., and Jespersen, D. C., The Design and Application of Upwind Schemes onUnstructured Meshes. *AIAA Paper 89-0336*, 1989.

Degrez, G., and Van Der Weide, E., Upwind Residual Distribution Schemes for Chemical Non-Equilibrium Flows. *AIAA Paper 99-3366*, 1999.

Fox, R. W., and McDonald, A. T., *Introdução à Mecânica dos Fluidos*, Guanabara, 1988.

Hirsch, C., *Numerical Computation of Internal and External Flows – Computational Methods for Inviscid and Viscous Flows*, John Wiley & Sons Ltd, 691p, 1990.

Liou, M., and Steffen Jr., C. J., A New Flux Splitting Scheme. *Journal of Computational*
Physics, 107: 23-39, 1993.

Liu, M., and Vinokur, M., Upwind Algorithms for General Thermo-Chemical Nonequilibrium Flows. *AIAA Paper 89-0201*, 1989.

Long, L. N., Khan, M. M. S., and Sharp, H. T., Massively Parallel Three-Dimensional Euler / Navier-Stokes Method. *AIAA Journal*, 29(5): 657-666, 1991.

Maciel, E. S. G., Relatório ao Conselho Nacional de Pesquisa e Desenvolvimento Tecnológico (CNPq) sobre as Atividades de Pesquisa Desenvolvidas no Primeiro Ano de Vigência da Bolsa de Estudos para Nível DCR-IF Referente ao Processo No. 304318 / 2003-5. *Technical Report, National Council of Scientific and Technological Development (CNPq)*, Recife, PE, Brazil, 37p, 2004.

Maciel, E. S. G., Analysis of Convergence Acceleration Techniques Used in Unstructured Algorithms in the Solution of Aeronautical Problems – Part I. *Proceedings of the XVIII International Congress of Mechanical Engineering (XVIII COBEM)*. Ouro Preto, MG, Brazil, 2005a.

Maciel, E. S. G., Relatório ao Conselho Nacional de Pesquisa e Desenvolvimento Tecnológico (CNPq) sobre as Atividades de Pesquisa Desenvolvidas no Segundo Ano de Vigência da Bolsa de Estudos para Nível DCR-IF Referente ao Processo No. 304318 / 2003-5. *Technical Report, National Council of Scientific and Technological Development (CNPq)*, Recife, PE, Brazil, 54p, 2005b.

Maciel, E. S. G., Analysis of Convergence Acceleration Techniques Used in Unstructured Algorithms in the Solution of Aerospace Problems – Part II. *Proceedings of the XII Brazilian Congress of Thermal Engineering and Sciences (XII ENCIT)*. Belo Horizonte, MG, Brazil, 2008.

Maciel, E. S. G., Relatório ao CNPq (Conselho Nacional de Desenvolvimento Científico e Tecnológico) sobre as atividades de pesquisa realizadas no período de 01/07/2008 até 30/06/2009 com relação ao projeto PDJ número 150143/2008-7. *Technical Report, National Council of Scientific and Technological Development (CNPq)*, São José dos Campos, SP, Brazil, 102p, 2009.

Maciel, E. S. G., and Pimenta, A. P., Reentry Flows in Chemical Non-Equilibrium in Two-Dimenions. *Proceedings of the X International Symposium on Combustion and Energy Utilization (ICCEU 2010)*, Mugla, Turkey, 2010. (http:/www.kampushaber.org/mugla-universitesi/the-10th-icceu-2010-international-conference-on-combustion-and-energy-utilization-programme-4743.html).

Radespiel, R., and Kroll, N., Accurate Flux Vector Splitting for Shocks and Shear Layers. *Journal of Computational Physics*, 121: 66-78, 1995.

Saxena, S. K., and Nair, M. T., An Improved Roe Scheme for Real Gas Flow. *AIAA Paper 2005-587*, 2005.

Van Leer, B., Flux-Vector Splitting for the Euler Equations. *Lecture Notes in Physics*. Springer Verlag, Berlin, 170: 507-512, 1982.